PHYSICAL REVIEW E **95**, 042208 (2017)

Mixing and the fractal geometry of piecewise isometries

Paul P. Park and Thomas F. Lynn
Department of Engineering Sciences and Applied Mathematics, Northwestern University, Evanston, Illinois 60208, USA

Paul B. Umbanhowar
Department of Mechanical Engineering, Northwestern University, Evanston, Illinois 60208, USA

Julio M. Ottino
Department of Chemical and Biological Engineering, Department of Mechanical Engineering, Northwestern University, Evanston, Illinois 60208, USA
and The Northwestern Institute on Complex Systems (NICO), Northwestern University, Evanston, Illinois 60208, USA

Richard M. Lueptow[*]
Department of Mechanical Engineering, Department of Chemical and Biological Engineering, Northwestern University, Evanston, Illinois 60208, USA
and The Northwestern Institute on Complex Systems (NICO), Northwestern University, Evanston, Illinois 60208, USA

(Received 13 December 2016; published 14 April 2017)

Mathematical concepts often have applicability in areas that may have surprised their original developers. This is the case with piecewise isometries (PWIs), which transform an object by cutting it into pieces that are then rearranged to reconstruct the original object, and which also provide a paradigm to study mixing via cutting and shuffling in physical sciences and engineering. Every PWI is characterized by a geometric structure called the exceptional set, E, whose complement comprises nonmixing regions in the domain. Varying the parameters that define the PWI changes both the structure of E as well as the degree of mixing the PWI produces, which begs the question of how to determine which parameters produce the best mixing. Motivated by mixing of yield stress materials, for example granular media, in physical systems, we use numerical simulations of PWIs on a hemispherical shell and examine how the fat fractal properties of E relate to the degree of mixing for any particular PWI. We present numerical evidence that the fractional coverage of E negatively correlates with the intensity of segregation, a standard measure for the degree of mixing, which suggests that fundamental properties of E such as fractional coverage can be used to predict the effectiveness of a particular PWI as a mixing mechanism.

DOI: 10.1103/PhysRevE.95.042208

I. INTRODUCTION

Mixing by cutting and shuffling, described mathematically as piecewise isometries (PWIs), is far less understood than other forms of mixing such as mixing generated by stretching and folding, which is directly applicable to fluids and can be cast in the language of nonlinear dynamics and chaos theory. Nevertheless, mixing with PWIs has potential for application in engineering processes involving granular materials [1–3], yield stress fluids, valved fluid flows [4,5], or flows with shear-banding materials, as well as for understanding certain notable geophysical phenomena (e.g., imbricate thrust faults [6]). PWIs follow simple rules that generate complex dynamics [7–20]. We focus here on measuring intrinsic features of PWIs and the mixed state of the system in order to establish a relationship between the theoretical properties of PWIs and mixing in practice.

There are various similar definitions of a PWI [21–24]; we define a PWI mapping M on a domain or space S as follows:

Definition 1. $M : S \to S$ such that the action of M on each partition element P_i of S is a Euclidean isometry (composition of translation, rotation, reflection, etc.). P_i, a closed region (including boundaries), is one of a finite number N partition elements of S, i.e., $\cup_{1 \leqslant i \leqslant N} P_i = S$, and where $P_i \cap P_j$ is measure zero for $i \neq j$.

A lower hemispherical shell (HS) undergoing a PWI transformation is split into four partition elements [bottom view, Fig. 1(a)], which are then rearranged into another HS [Fig. 1(b)]. We let $\mathcal{D}$ denote the set of all such borders that partition S [black and red arcs in Fig. 1(a)]:

Definition 2. $\mathcal{D} = \cup_{i,j}(P_i \cap P_j)$ for $i \neq j$.

Note that since each segment of $\mathcal{D}$ is in the shared domain of two isometries, the map M is multivalued on $\mathcal{D}$.

In this study we focus on a particular class of PWIs that result from successive rotations about the z and x axes by θ_z and θ_x, with periodic boundaries at the hemispherical edge (Fig. 2). The operation is expressed mathematically by Sturman *et al.* [17] and is applied here for computer simulations of PWIs. This class of PWIs is specified by the ordered pair (θ_z,θ_x) and approximates the effect of an infinitely thin flowing layer in a spherical granular tumbler [2,3,17,26], which can be reduced to two-dimensional dynamics on the HS. The ordered pair (θ_z,θ_x) is referred to as a protocol for the remainder of this paper, and it determines the location of $\mathcal{D}$ [for instance, the set $\mathcal{D}$ in Fig. 1(a) derives from the $(45^\circ,45^\circ)$ protocol].

We can observe mixing on the HS when a particular PWI is repeated, with the rate and degree of mixing depending on

---

[*] r-lueptow@northwestern.edu

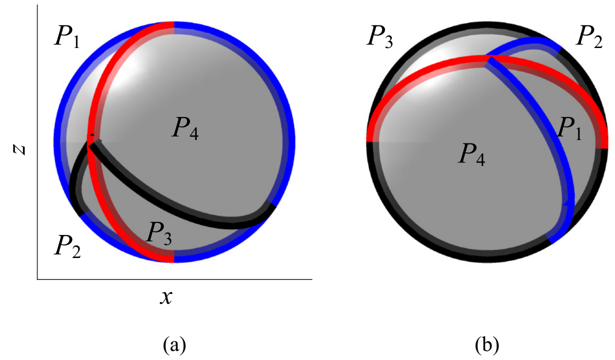

FIG. 1. Bottom view of a hemispherical shell (HS) showing (a) the initial location of the pieces to be rearranged, P_i, and their corresponding boundaries comprising $\mathcal{D}$ (black and red arcs) and the domain boundary, ∂S (blue arc) and (b) their subsequent locations after their rearrangement by one iteration of the PWI. Reproduced from Park *et al.* [25] with permission from AIP Publishing.

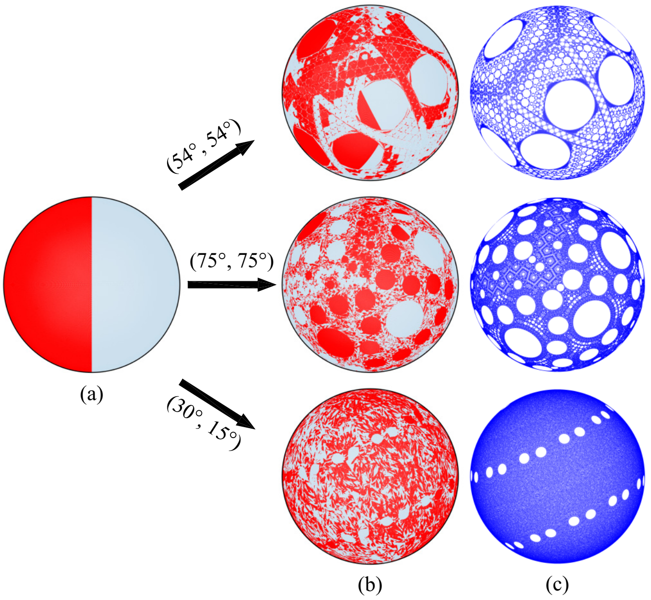

FIG. 3. Bottom view of (a) initial condition of seeded colors on the HS, (b) mixing on the HS for the (54°,54°), (75°,75°), and (30°,15°) protocols after $m = 150$ iterations, and (c) E for corresponding protocols obtained by tracking the respective $\mathcal{D}$ for 5000 iterations.

the protocol. This is demonstrated in Fig. 3(b), where the three protocols (54°,54°), (75°,75°), and (30°,15°) result in vastly different degrees of mixing after $m = 150$ iterations for the HS initially colored half red and half light blue in Fig. 3(a) (this and all remaining figures with a HS show the bottom view of the HS).

When considering mixing under PWIs, nonmixing regions can be identified by visualizing the exceptional set [23]:

Definition 3. $E = \bigcup_{-\infty<i<\infty} M^i\mathcal{D}$.

The dynamics on the closure of E has been shown to be ergodic in other systems [27–30], and we conjecture that this is also the case here, which is why, for ease of illustration, we approximate E with its subset E_+ [25]:

Definition 4. $E_+ = \bigcup_{1\leqslant i<\infty} M^i\mathcal{D}$.

All images representing E hereafter are approximated with E_+. We generate E_+ by seeding tracer points on an equivalent substitute of $\mathcal{D}$ (refer to [25] for further details) and recording their trajectories for a large number of iterations [Fig. 3(c)]. The white areas in the HS are nonmixing regions known as cells [31,32] (we refer to the region as a cell rather than the set of points occupying the region as in [25]), which form a subset of the complement of the closure of E. In Fig. 3(c) it is evident that the cells coincide with nonmixing regions in Fig. 3(b) for the (54°,54°) and (75°,75°) protocols. For example, the four large circular cells in Fig. 3(c) for the (75°,75°) protocol correspond to large light blue and red circular regions in Fig. 3(b). For the (54°,54°) protocol, there are two adjacent circular regions in Fig. 3(b) located near the center and just below that contain both red and light blue colors with a clear divide between the two. This is because the initial seeding of colors overlaps with two of the cells shown in Fig. 3(c) and both colors happened to be seeded in each of the cells.

Colors contained inside a cell are said to have a *periodic itinerary* [31,32] because they travel as a group from one cell to others of the same size before returning to the cell where they originated, but with a rotation. The boundaries between the two colors in the cells for the (54°,54°) protocol are slanted rather than in the vertical orientation of the initial condition due to this rotation. The mixing patterns of the (54°,54°) and (75°,75°) protocols demonstrate that cells are nonmixing because no colors penetrate them and no mixing occurs within them.

While a greater coverage of E seems to produce qualitatively better mixing in each example in Fig. 3, our goal is to show that such a relationship exists more generally based on quantifying the fractional coverage of E and comparing

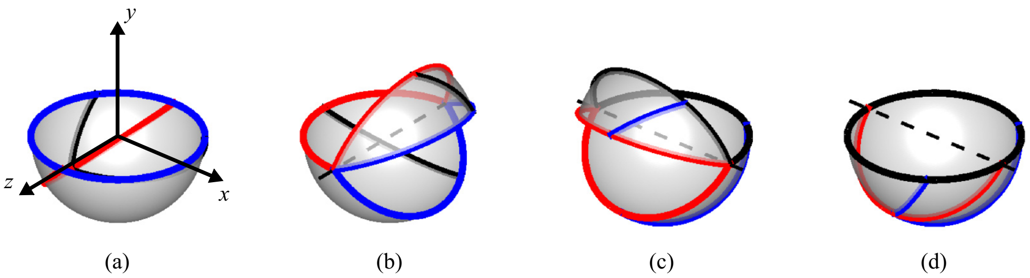

FIG. 2. PWI operation on the HS for $(\theta_z,\theta_x) = (45°,45°)$. Dashed lines indicate the two rotation axes. (a) Initial condition. (b) Rotation and cut about the z axis by θ_z. (c) Rotation and cut about the x axis by θ_x. (d) New state after one iteration. Adapted from Park *et al.* [25] with permission from AIP Publishing.

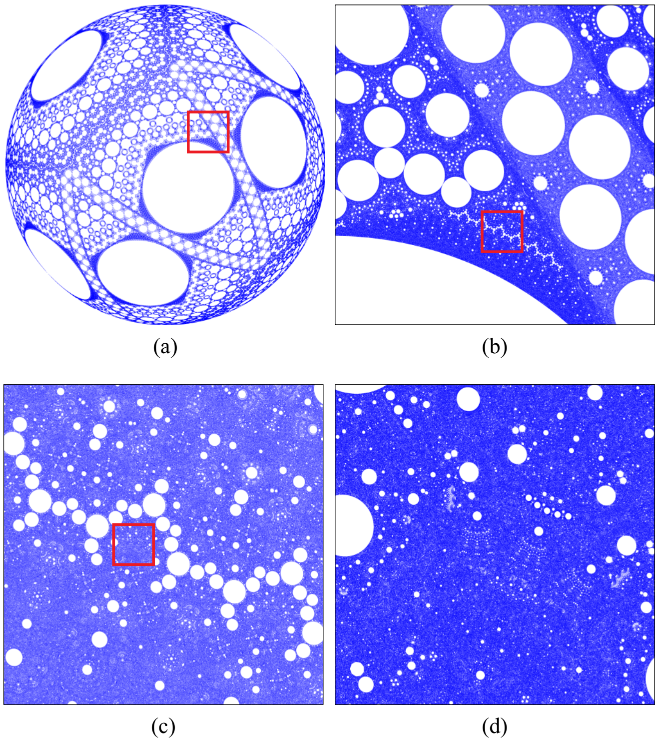
(a) (b) (c) (d)

FIG. 4. Magnifying E for the (54°,54°) protocol by 8× to various scales. Each magnification, from (a) to (b), from (b) to (c), and from (c) to (d), of the red box reveals circular cells at progressively finer scales.

the coverage to standard measures for the degree of mixing. If greater coverage of E produces better mixing, this would imply that measures of fundamental properties of E exist which can be used to judge the general effectiveness of a particular PWI as a mixing mechanism. Quantifying the fractional coverage of E and the degree of mixing, each has its respective complications and factors that need to be considered, which are mentioned here and addressed more thoroughly in the following sections.

First, we observe that the approximated E has two distinct and related features: Fine details emerge when E is viewed at magnified scales (Fig. 4), and the apparent coverage depends on the resolution at which E is measured, described succinctly by Umberger and Farmer as "structure on all scales" and "dependence of the apparent size on the scale of resolution" [33], all of which are features that characterize fractals. For most of the cases considered here, E appears to have positive area, which suggests that they are *fat fractals*, as opposed to traditional fractals which are measure zero, i.e., they have zero area in two dimensions [33].

Note, however, that although E in Fig. 3(c) appears to fill in some regions while leaving others empty, E is made up of arcs having length but no thickness (it is a countable union of measure-zero sets). Thus, even regions that are dark blue in Fig. 3(c) consist of densely packed curves with zero thickness that are approximated by densely packed points in practice. That E exhibits fractal characteristics allows us to quantify the area that E appears to cover using a box counting method [34], but by doing so, we are in effect "fattening" E and measuring its closure $\bar{E}$ [35,36]. For the remainder of this paper, we use the term "fractional coverage of E" with the understanding that the term refers to the measure of $\bar{E}$. Aside from our conjecture that E is a fat fractal, which gives us a possible method for measuring its coverage, it is significant that the amount of mixing with PWIs could be connected to the fractal characteristics displayed by E for a particular protocol, given the close relationship between fractals and mixing of fluids [37–46].

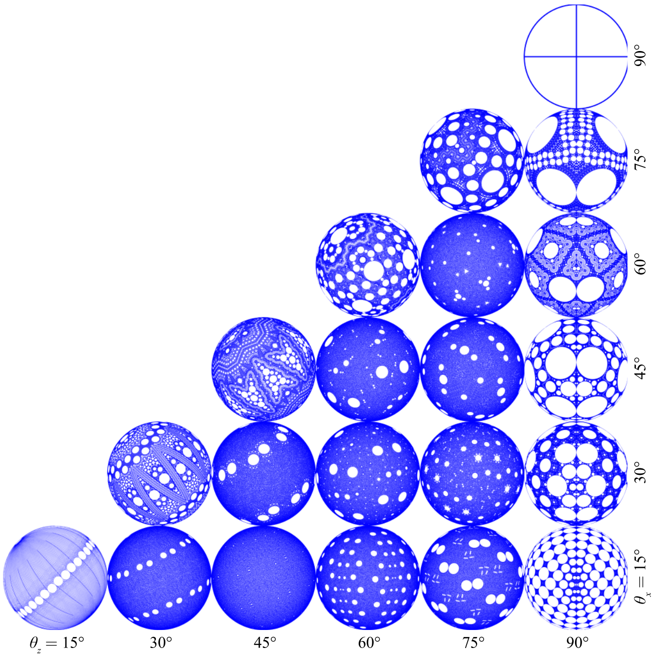

FIG. 5. Visualizing E with $m = 5000$ for θ_z and $\theta_x \in [15°,90°]$ varying in 15° increments (bottom view). Reproduced from Park *et al.* [25] with permission from AIP Publishing.

Considering a range of protocol values, Fig. 5 shows that a variety of intricate patterns is possible for E, where E is approximated at $m = 5000$ for values of θ_z and θ_x ranging from 15° to 90° in 15° increments. Only protocols with $\theta_x \leqslant \theta_z$ are shown because the global structures of E for the (θ_1,θ_2) and (θ_2,θ_1) protocols are symmetric (see Appendix A). Further exploration of these patterns for smaller angle increments suggests a rich variety of patterns for E (see Figs. 17–19).

The coverage of E also varies substantially with the choice of protocol. The coverage ranges from apparently completely filled for the (45°,15°) protocol to nearly empty for the (90°,90°) protocol. The (90°,90°) protocol represents a trivial case where the partition of the HS for the next iteration overlaps perfectly with the reassembled HS after an iteration of the protocol (the four cells have a periodic itinerary of 2 but are period 6 because each cell has three sides that the rotation of the cell aligns to). Visible coverage is affected by the size and number of cells. The observed cells are frequently circular, with the exception of the (90°,90°) protocol, whose three-sided cells appear polygonal, which suggests the possibility of other protocols that share similar features. Circles of different sizes nearly fill the HS for the (90°,45°) protocol, while circles of similar size nearly fill the HS for the (90°,15°) protocol. The (90°,75°) protocol has four large circles along with many small circles of similar size that form a band on the HS. Compared to

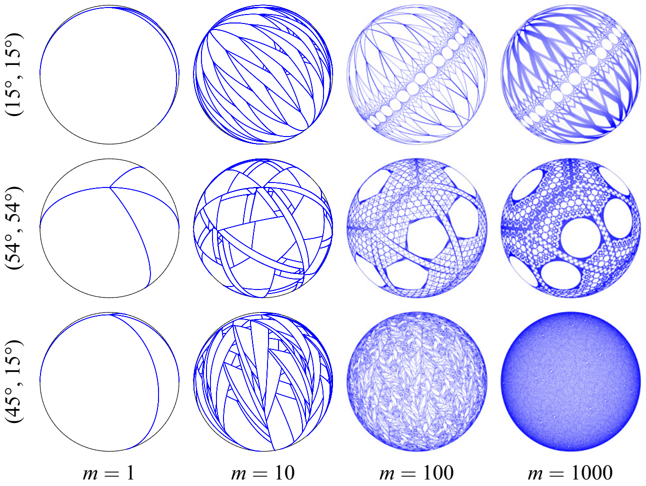

FIG. 6. Progression of the approximation of E as a function of the number of protocol iterations m (bottom view). Note that E for the (15°,15°) protocol at $m = 1000$ is not fully developed.

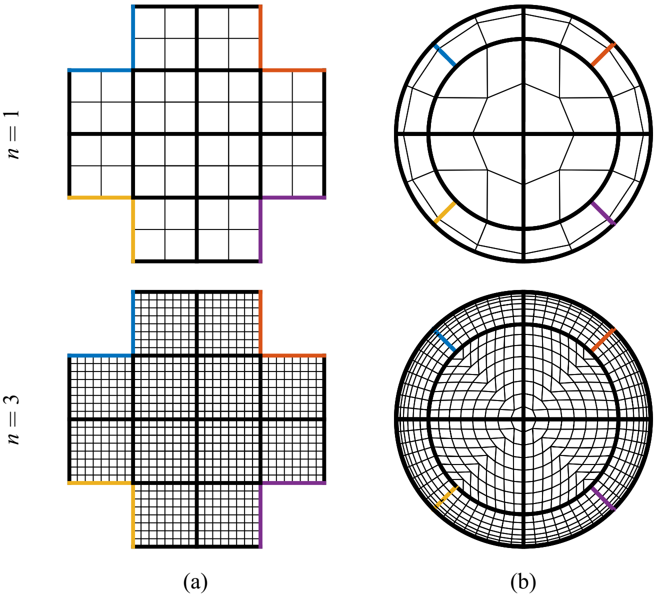

FIG. 7. (a) An unfolded isocube half whose resolution for a quarter of one face is 2×2 (top) and $2^3 \times 2^3$ (bottom). The total number of boxes is $N = 12 \times 2^n \times 2^n$, since there are 12 quarter faces (each quarter face is outlined with bold lines). (b) Isocube half in (a) mapped to the HS as viewed from the bottom.

those with $\theta_z = \theta_x$ or $\theta_z = 90°$, the other protocols generally have greater coverage and smaller cells.

It is important to note that while PWIs are "nonmixing" according to mathematical definitions [27–30], it is possible to compare the mixed states of protocols using mechanical definitions. Measuring the degree of mixing is complicated by mechanical factors such as the choice of initial condition of the seeded colors, the number of points used in mixing simulations, and, for most measures of mixing such as the *intensity of segregation* [47] that we used to measure mixedness, the resolution of the grid on which the measure is calculated.

In this paper, we quantify the coverage of E over the HS using the box counting method [33,35,36,48] and show that for most protocols E is well described as a fat fractal. We compare these characteristics to the degree of mixing achieved via numerical simulations, quantified by an established engineering measure known as the intensity of segregation [47], to demonstrate a general relationship between the fat fractal characteristics of E and mixing with PWIs.

II. APPROXIMATING *E*

The choice of $m = 5000$ for approximating E in Figs. 5 and 17–19 is arbitrary and, consequently, must be addressed to ensure that we derive reliable measures of its characteristics. This issue is highlighted in Fig. 6 where the "filling" by $\mathcal{D}$ is shown for various protocols after $m = 1$, 10, 100, and 1000 iterations. For the (15°,15°) protocol, the trajectory of $\mathcal{D}$ cuts the HS into thin slices initially at $m = 10$, but at $m = 100$ and $m = 1000$, the orbit is in close proximity to past trajectories and fills the HS slowly while leaving a band of cells on the diagonal. The (54°,54°) protocol features several pentagons initially, which fill in to become large circular cells. At $m = 100$ and $m = 1000$, the (54°,54°) protocol fills the HS more evenly, with many small cells in addition to large cells. The trajectory of $\mathcal{D}$ for the (45°,15°) protocol cuts the HS into thin slices like the (15°,15°) protocol initially, but fills the HS uniformly without any visible cells at $m = 1000$ iterations.

The issue of choosing a particular value of m to approximate E is highlighted using Fig. 6 as an example. For the (54°,54°) and (45°,15°) protocols, the points that are followed after $m = 1000$ fill the HS more densely with more iterations, but the qualitative structure of E changes little. In contrast, for the (15°,15°) protocol, we conclude that the structure of E is incomplete after $m = 1000$ compared to the $m = 5000$ approximation shown in Fig. 5 (bottom left corner). At $m = 5000$, the structure appears complete based on how densely the points fill the space.

Two points are evident from Fig. 6. First, from a visual perspective, the structure that emerges from the orbit of $\mathcal{D}$ seems to reach an "asymptotic state" for some sufficiently large value of m. Second, the value of m at which the general structure of E is revealed varies with the protocol. For the (45°,15°) protocol, $m = 1000$ might suffice, whereas $m \geqslant 5000$ may be necessary for other protocols such as (15°,15°).

If numerous protocols are to be studied, this leads to the question of how to automate the process of determining m such that enough information is obtained from the orbit of $\mathcal{D}$ to generate a reasonable approximation of the coverage of E. We determine whether the coverage of E is close to an asymptotic state based on the ability of points to visit new regions of the HS. To achieve this, we use the bottom half of an *isocube* as shown in Fig. 7 to discretize the HS in a near-uniform manner (each box in the grid is the same size, and its shape is distorted only slightly when mapped on the HS) [49]. We conclude that an asymptotic state has been reached when the points that are seeded to generate E fail to visit a new box in the chosen grid for a specified number of *consecutive* iterations. After each

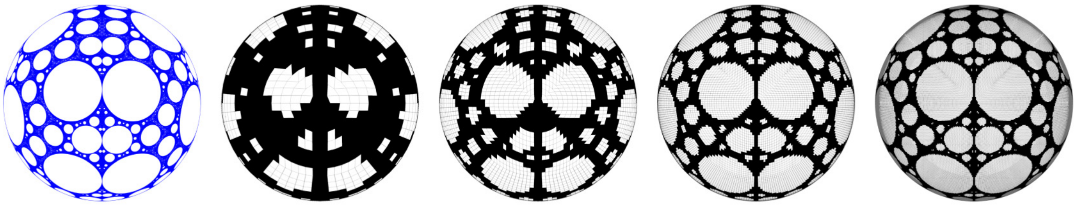

FIG. 8. Measuring the fraction of coverage of E for the (90°,45°) protocol at resolutions of $n \in \{3,4,5,6\}$. Boxes that contain portions of E are black (bottom view).

iteration, all boxes containing a point are marked as occupied, and if all seeded points fail to visit a new box for a set number of consecutive iterations, then, for the purpose of this study, we conclude that there is no more information to be gained regarding the coverage of E at that grid resolution.

Before applying this approach, we briefly describe the grid of the isocube half. Figure 7(a) shows an unfolded isocube half. The blue, orange, purple, and yellow colors have two edges, and when "glued" together with their respective colors, the unfolded isocube half forms the bottom half of a cube. The bold black lines on the outside form the outer edge of the assembled half cube, and the inner bold black lines discretize the domain into 12 quarter faces (we refer to them as quarter faces because the bottom face would be divided into four squares). Each quarter face is further discretized with a $2^n \times 2^n$ grid (fine black lines), such that the total number of boxes on the isocube is $N = 12 \times 2^n \times 2^n$. The resolution of the grid is denoted by the exponent n. This isocube half can then be mapped to the HS to form an area-preserving grid as shown in Fig. 7(b). All boxes have equal area, and the individual box area goes to zero in the limit of $N \to \infty$. See [49] for details of the isocube transformation.

The grid and its resolution are critical to several aspects of the numerical simulations, such as choosing the number of points to seed for $\mathcal{D}$, determining whether enough points are available for obtaining a reliable measure for the coverage of E, and, in Sec. IV, seeding points for mixing simulations and measuring the degree of mixing. The role of the grid is described in detail as we discuss each method.

For determining whether a numerical simulation reaches the asymptotic state for the structure E, the grid resolution is set to a maximum value of $n = 10$. At $n = 10$, there are approximately 1.25×10^7 boxes that can be visited by points on the HS. We approximate $\mathcal{D}$ as described by Park *et al.* [25], with two sets of points near the edge of the HS: one set of points is seeded before the z-axis rotation [blue curve in Figs. 1(a) and 2(a)], and the other set of points is seeded before the x-axis rotation [red curve in Fig. 2(c)]. The points for each set are seeded in the center of boxes at the very edge of the HS (one point per box), which is approximately 8000 points (there are eight quarter faces on the edge of the isocube half, and each quarter face has $2^{10} = 1024$ boxes on one edge). Thus, we follow the orbits of 16 000 points across a grid of 1.25×10^7 boxes. The structure of E is considered to be close to an asymptotic state when none of the 16 000 points visit a new box for 1000 consecutive iterations.

III. APPROXIMATING THE FRACTIONAL COVERAGE OF E WITH BOX COUNTING

The approximation of E is closely tied to measuring its fractional coverage: the number of boxes visited by the end of the simulation divided by the total number of boxes is an approximation of the fractional coverage at a given resolution. Also, if the approximation of E is judged to have reached an asymptotic state on a high resolution grid ($n = 10$), then there must be enough points on the HS that the coverage of E can be measured for lower resolutions, i.e., $n < 10$, which is additional information that can be used for further analysis. Let Φ_n denote the fraction of boxes occupied by E for a grid discretizing the HS with resolution n. This is illustrated for the (90°,45°) protocol in Fig. 8, which shows how Φ_n changes for different values of n. A finer grid yields a more "accurate" measure, and this naturally leads to the question of what the appropriate resolution should be to measure E. If possible, taking $n \to \infty$ to determine Φ_∞ would be ideal.

Considering the fractional coverage Φ_n for six sample protocols and $2 \leqslant n \leqslant 10$, Fig. 9 shows that Φ_n generally decays toward an asymptotic value. We fit the points in Fig. 9 to a curve to approximate a value for Φ_∞. The choice for the curve is based on the observation that E typically resembles a fat fractal. Thus, the following equation is used to fit Φ_n for

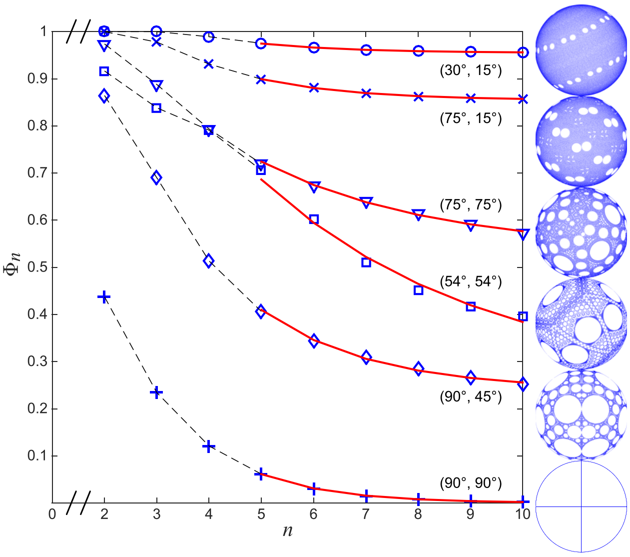

FIG. 9. Fitting the measured values of Φ_n for various protocols. Corresponding E shown on the right.

TABLE I. Fitted fat fractal coefficients and goodness of fit.

Protocol	Φ_∞	d_{ext}	R^2
(45°,15°)	0.996	1.674	0.868
(30°,15°)	0.955	1.201	0.999
(75°,15°)	0.854	1.223	1.000
(75°,75°)	0.535	1.563	0.998
(89°,52°)	0.319	1.077	1.000
(54°,54°)	0.250	1.660	0.993
(90°,45°)	0.240	1.322	0.999
(90°,90°)	0.000	1.014	1.000
(72°,1°)	0.000	1.921	0.872

each protocol [33,36]:

$$\Phi_n = \Phi_\infty + Ae^{-Bn}, \tag{1}$$

where $\lim_{n\to\infty} \Phi_n = \Phi_\infty$ is the asymptotic fractional coverage.

The *exterior dimension* can be calculated for each E from the coefficient of n in Eq. (1) [33,35,48]:

$$d_{\text{ext}} = 2 - \frac{B}{\ln 2}. \tag{2}$$

We calculate the exterior dimension rather than the traditional Hausdorff dimension, which yields a value of 2 for fat fractals and does not provide information about the multiscale structure observed for E.

The built-in trust-region-reflective algorithm [50,51] in MATLAB is used to fit the data to Eq. (1) (starting from $n = 5$, because low resolutions give poor approximations to Φ_∞), which gives the fractional coverage Φ_∞ and exterior dimension d_{ext} for each case (Table I). The quality of the fit is measured by the R^2 value (goodness of fit) which ranges from zero to 1, where 1 indicates that there is no difference between the data and fitted values. A constraint that $\Phi_\infty \geqslant 0$ and $B \leqslant \ln 2$ is also applied to the curve fit based on heuristics (we expect $\Phi_n \geqslant 0$ for all n and $d_{\text{ext}} \geqslant 1$ for a fat fractal). Given the nature of the fit and these constraints, $0 \leqslant \Phi_\infty \leqslant 1$ and $1 \leqslant d_{\text{ext}} \leqslant 2$. As anticipated from visual inspection, the fractional coverage of the exceptional sets on the right of Fig. 9 decreases monotonically from close to 1 for the (30°,15°) protocol (top) to zero for the (90°,90°) protocol (bottom). In contrast, the connection between the values of d_{ext} and E is not obvious. Note that as expected, for the (90°,90°) protocol, Φ_∞ is approximately zero and $d_{\text{ext}} \sim 1$ because E for this protocol is composed of just two arcs.

For the (45°,15°) protocol (not shown in Fig. 9) E appears to cover the entire HS (Figs. 5 and 6), and Φ_∞ is close to 1, but the R^2 value is relatively low (Table I). This occurs because the (45°,15°) protocol generates cells that are nearly all smaller than the box size for a grid of $n \leqslant 5$, which means $\Phi_n = 1$ for $n < 5$. Consequently, a scaling behavior is only observed starting from $n = 5$ in this case, and higher resolutions ($n > 10$) would be necessary for a better fit to Eq. (1). In other cases, the data may not scale as Eq. (1) immediately, as is illustrated by the dashed lines connecting the data points of $n < 5$ for (75°,15°), and (54°,54°) in Fig. 9. The values of Φ_n are decreasing for the (75°,15°) and (54°,54°) protocols, but an inflection point exists at $n^* = 3$ and $n^* = 4$, respectively [uncharacteristic of Eq. (1)], which can lead to lower R^2 values. In this study, θ_z was varied from 1° to 90° in 1° increments, and θ_x was varied from 1° to θ_z in 1° increments for a given θ_z (reasons stated in Sec. I), for a total of 4095 protocols. Approximately 80% of the protocols had $R^2 \geqslant 0.9$. For ones with $R^2 < 0.9$, most, if not all, had $\Phi_\infty \geqslant 0.95$, indicating a very high coverage of the HS by E.

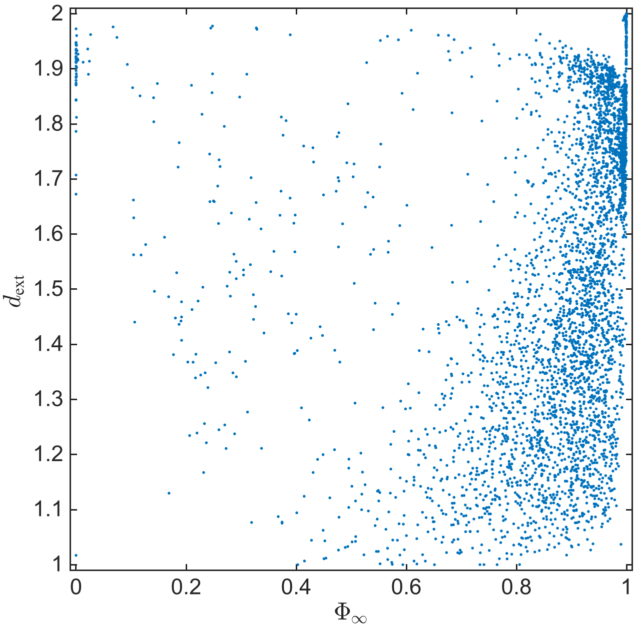

FIG. 10. No obvious correlation between the asymptotic coverage Φ_∞ and exterior dimension d_{ext} exists for the 4095 protocols examined.

A key question is the relation between the fractional coverage and fractal dimension. Figure 10 shows the fitted values for Φ_∞ and d_{ext}. More than 90% of the Φ_∞ values are greater than 0.6, and 60% of the Φ_∞ values are greater than 0.9. The values of d_{ext} are spread relatively uniformly, and there is no obvious relationship between Φ_∞ and d_{ext}.

IV. COMPARING Φ_∞ TO THE DEGREE OF MIXING

In this section, Φ_∞ is compared to the degree of mixing to determine whether the relationship observed based on visual comparison in Sec. I, i.e., that a greater fractional coverage of E results in better mixing, is also reflected in standard metrics. To simulate mixing on the HS, the left half of the HS is seeded with points associated with species 1 (red), and the right half with species 2 (light blue), as in Fig. 3(a). Points were seeded in the center of each box for a grid resolution of $n = 8$, which is approximately 8×10^5 points. Let $\bar{c}$ denote the average concentration of species 1. While concentration is calculated based on the frequency of points divided by the total number, it is meant to represent a fraction of an area of the surface. Here, mixing at each iteration m is measured on a grid of N boxes using the intensity of segregation $\mathcal{I}(m)$ [47]:

$$\mathcal{I}(m) = \frac{1}{\bar{c}(1-\bar{c})}\left(\frac{1}{N}\sum_{i=1}^{N}(c_i(m)-\bar{c})^2\right) \in [0,1], \tag{3}$$

where $c_i(m)$ is the local concentration of species 1 in box i of the grid at iteration m, and $\mathcal{I}$ represents the normalized variance in the local concentration of species 1 across all N boxes. If the domain is uniformly mixed for a given resolution, then $c_i(m) = \bar{c}$ for all i, and there is no variance, i.e., $\mathcal{I} = 0$. If the domain is completely unmixed (segregated), then $c_i(m) = 1$ or zero in each bin, and the variance is at its maximum value of $\bar{c}(1-\bar{c})$, so $\mathcal{I} = 1$. Note that for cells with distinct discontinuities, e.g., as shown in Fig. 3(b) for the (54°,54°) protocol, if the grid resolution is high enough that the boxes are smaller than the cells, boxes that do not contain the discontinuity will only be occupied by one species. This implies that the local concentration will be zero or 1, and boxes along the discontinuity will contain a mix of species. We use a grid resolution of $n = 3$, which corresponds to $N = 768$ boxes in the grid. Simulations were run for the same set of 4095 protocols described in Sec. III.

Note that $\mathcal{I}$ depends on the resolution of the grid on which it is measured and the total number of points seeded on the HS. For a set number of points, if the grid resolution increases, then the measured segregation will increase as well. If the resolution is such that the number of boxes equals the number of points (i.e., given that each point maintains its distance from neighboring points due to the isometry, only one point should occupy a box), then $\mathcal{I} = 1$ because the concentration of species 1 in each box will be zero or 1. On the other hand, if the grid resolution decreases, then the measured segregation will decrease until it reaches zero when the grid consists of one box. In both extremes, $\mathcal{I}$ is not a meaningful measure of the mixed state of the system.

A grid resolution of $n = 3$ and 8×10^5 points were chosen in consideration of the issues mentioned above while being mindful of computational limitations. There is a sufficient number of points in each box (approximately 1000 points per box) to ensure statistically reasonable results, while there is also a sufficient number of boxes to yield a measurement that reflects the mixed state of the entire HS.

For six sample protocols, $\mathcal{I}$ decreases over 1000 iterations (Fig. 11). After approximately 500 iterations, $\mathcal{I}$ reaches a "steady" state for the (89°,52°), (54°,54°), (75°,75°), and (30°,15°) protocols, characterized by an asymptotic trend as m increases. A steady state also appears likely for the (75°,15°) protocol for more than 1000 iterations, but it is unclear if there is a steady state for the (72°,1°) protocol. Perhaps what is more interesting is the ordering of $\mathcal{I}$ for different protocols when compared to the asymptotic fractional coverage Φ_∞ for E. With the exception of the (72°,1°) and (89°,52°) protocols, the apparent coverage of E is in ascending order from top to bottom. Because materials in cells do not mix, this suggests that the measure Φ_∞ for E could indicate the ultimate degree of mixing, i.e., a protocol with a higher Φ_∞ should lead to better mixing and less segregation than a protocol with a lower Φ_∞.

The (72°,1°) protocol is one of possibly several exceptions that behaves unlike the other protocols shown in Fig. 11. Its zero Φ_∞ value (Table I) suggests that mixing is unlikely for this particular protocol, but its $\mathcal{I}$, while oscillating, is steadily decreasing, indicating that mixing is occurring, albeit slowly. It would seem to continue if the simulation were run for longer than 1000 iterations. Thus, the measures Φ_∞ and $\mathcal{I}$ are evidently at odds in this case.

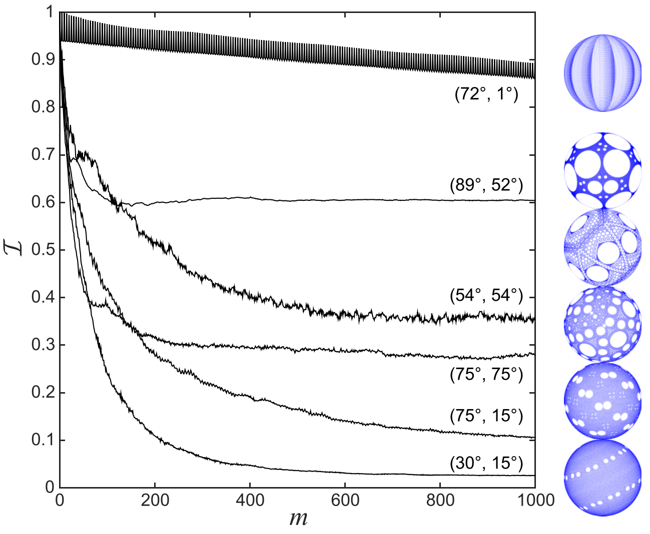

FIG. 11. Intensity of segregation $\mathcal{I}$ versus iteration number for six sample protocols; corresponding E are shown on the right.

We speculate that this discrepancy comes about because the cells of the (72°,1°) protocol are minuscule. The cells appear consistent in size, and each cell is approximately ten times smaller than a single box of the grid. While it is understood that no mixing occurs within a cell, the cells of the (72°,1°) protocol are small enough that they can each be considered an individual particle, in contrast to that for protocols with large cells such as the (90°,90°) protocol. The mixing that is measured by $\mathcal{I}$ results from the rearranging of the minuscule cells of different colors in each box.

The (89°,52°) protocol appears to be another exception, compared to the (54°,54°) protocol, possibly again relating to cell sizes. While its fractional coverage of E may be greater ($\Phi_\infty = 0.319$ compared to 0.250 from Table I), the prominent cells of the (89°,52°) protocol are much larger and more numerous than that of the (54°,54°) protocol, whose remaining cells other than the several large cells happen to be fairly small. The (89°,52°) protocol underperforms compared to what its Φ_∞ value would suggest because of its particular distribution of cell sizes.

While $\mathcal{I}$ does not reach an asymptotic state by $m = 1000$ for some protocols, our goal is to determine whether most of the protocols tested indeed reach their respective asymptotes. We take a simple approach to examining this by considering the standard deviation of $\mathcal{I}$, denoted $\sigma(\mathcal{I})$, over a set span of iterations. For a given protocol, if $\mathcal{I}$ reaches an asymptotic state, the set of preceding iterations should have similar values of $\mathcal{I}$, leading to $\sigma(\mathcal{I}) \sim 0$. If this is the case for most protocols, then the distribution of $\sigma(\mathcal{I})$ will be narrow and close to zero for later iterations.

The distributions of $\sigma(\mathcal{I})$ over a span of 50 iterations ($s = 50$) are shown in Fig. 12 for the 4095 protocols at various ranges of iterations. Figure 12(a) shows the distribution of $\sigma(\mathcal{I})$ on a linear scale. For $m \in [51,100]$, the distribution is wide and centered around 0.045. At higher iterations, the distribution of $\sigma(\mathcal{I})$ shifts closer to zero, indicating that $\mathcal{I}$ is essentially constant for most protocols by the end of the simulation, consistent with an asymptotic state. Figure 12(b) shows the

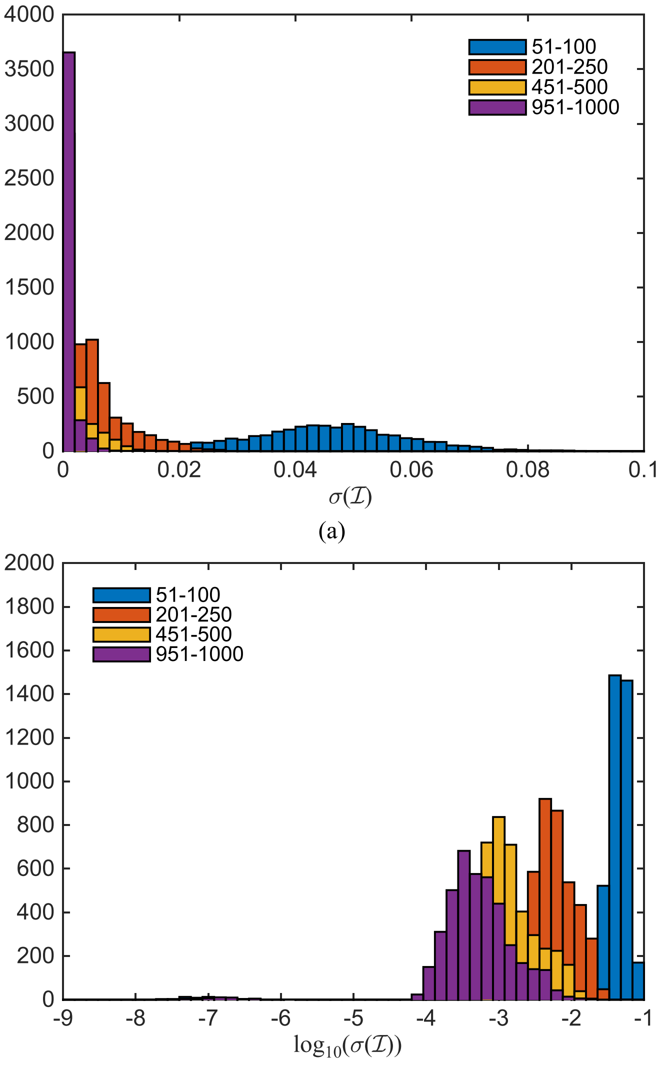

(a)

(b)

FIG. 12. Distribution of $\sigma(\mathcal{I})$ for all 4095 protocols over a range of $s = 50$ iterations at different m. There is some overlap between distributions for different ranges of iterations; the distribution of later iterations are plotted over earlier ones.

distribution of $\sigma(\mathcal{I})$ on a logarithmic scale, where most values are in the range $10^{-4} \leqslant \sigma(\mathcal{I}) \leqslant 10^{-2}$ for $m \in [951,1000]$. There is also a small group of protocols whose values of $\sigma(\mathcal{I})$ are orders of magnitude smaller than that of the rest of the population. The protocols in this group all have $\theta_z = 90^\circ$; i.e., the rotation about the z axis only flips the colors from one side to the other, producing no mixing. In theory, $\mathcal{I} = 1$ for all iterations in this case, which is why $\sigma(\mathcal{I}) \sim 0$ for all protocols with $\theta_z = 90^\circ$. Thus, this group of protocols has values of $\sigma(\mathcal{I})$ orders of magnitude smaller than that for the rest. This highlights the challenge of accounting for the impact of initial conditions in the study of mixing; however, this topic is beyond the scope of this paper.

Distributions of $\sigma(\mathcal{I})$ for other spans $s \in \{5,10,25,100\}$ were also calculated. These distributions also became narrower and tended towards zero for increased numbers of iterations, which reinforces the notion that, in general, $\mathcal{I}$ reaches a steady state by $m = 1000$ iterations. Distributions of the average change in $\mathcal{I}$, denoted $\overline{\Delta\mathcal{I}}$, for $s = 50$ at various ranges of iterations were examined to see if $\mathcal{I}$ trends in any direction. It was found that $\overline{\Delta\mathcal{I}}$ has a wide distribution with a negative mean initially, since $\mathcal{I}$ decreases for most protocols when mixing occurs, but at different rates. At higher iterations, the distribution of $\overline{\Delta\mathcal{I}}$ is narrower and shifts toward zero, indicating that $\mathcal{I}$ does not trend in a particular direction after its initial decrease. Again, this indicates that $\mathcal{I}$ at $m = 1000$ reaches steady state for most protocols and can be used to compare to Φ_∞, which is an intrinsic value of E.

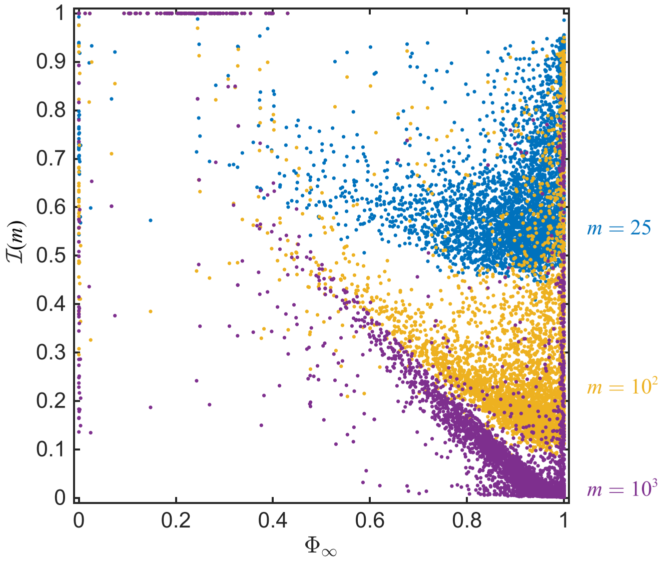

FIG. 13. Comparing $\mathcal{I}$ to Φ_∞ for all 4095 protocols at iterations $m = 25$, 10^2, and 10^3. At high m, $\mathcal{I}$ and Φ_∞ appear to be negatively, linearly correlated.

Returning now to the relationship between the asymptotic fractional coverage Φ_∞ of E and the traditional measure of mixing, the segregation index $\mathcal{I}$, Fig. 13 shows a scatterplot of $\mathcal{I}$ versus Φ_∞ at different numbers of iterations. Initially, all protocols start from $\mathcal{I} = 1$, but after each iteration, $\mathcal{I}$ decreases as mixing occurs. The points are broadly scattered for smaller m, but as m is increased, they appear to collapse toward a diagonal line. The negative linear correlation between $\mathcal{I}$ and Φ_∞ at $m = 1000$ confirms the hypothesis that the structure of E, specifically the asymptotic fractional coverage Φ_∞, can be a useful indicator of the degree of mixing. This is significant given the many factors involved with mixing and measuring the degree of mixing (e.g., species number, concentration, and initial distribution as well as the number of tracer points and the grid geometry and resolution for measuring $\mathcal{I}$). Materials in cells do not mix, and this is reflected in mixing simulations as well. Larger Φ_∞ corresponds to a smaller overall size of the nonmixing regions (cells). Thus, a negative correlation between $\mathcal{I}(m = 1000)$ and Φ_∞ results. Therefore, fractional coverage Φ_∞ of E can be a useful indicator for judging a particular protocol's effectiveness at mixing.

There are a few exceptions to the negative linear correlation between Φ_∞ and $\mathcal{I}$, one of which is the protocols with $\Phi_\infty \sim 1$ that maintain values of $\mathcal{I} > 0$ even after 1000 iterations along the right edge of Fig. 13. In comparing the points at the three different numbers of iterations as in Fig. 13, it is clear that the values of $\mathcal{I}$ are decreasing, which suggests the rate of mixing may be very slow for these protocols despite the high Φ_∞ value. While the fractional coverage of E predicts the long-term mixing achieved, it cannot predict the rate of mixing. Another exception is when the initial condition and protocol are such that no mixing will occur, e.g., when $\theta_z = 90^\circ$ and one species initially occupies the left half of the HS and the other species occupies the right half of the HS as was pointed out earlier. This is the set of points at $\mathcal{I} \sim 1$ along the top edge in Fig. 13 that do not collapse independent of m or Φ_∞. Finally, there is also a group of protocols near the left edge with $\Phi_\infty \sim 0$, but with decreasing values of $\mathcal{I}$. These are protocols whose behavior may be similar to the $(72^\circ, 1^\circ)$ protocol, which has $\Phi_\infty \sim 0$ and a steadily decreasing $\mathcal{I}$ for increasing m. These special cases point to the subtleties of studying mixing with PWIs, but also highlight the fact that, as a general rule, Φ_∞ can be used as a first-order type approximation for predicting the degree of mixing for PWIs.

V. CONCLUSION

When mixing with PWIs, the exceptional set, E, is an inherent structure on the domain that can be used to predict the overall degree of mixing that will be produced. Specifically, the fractional coverage of E, Φ_∞, shows a negative linear correlation with the intensity of segregation, $\mathcal{I}$, a standard measure for mixedness. Because the complement of E consists of cells (nonmixing regions), the fractional coverage Φ_∞ of the fat fractal geometry of E represents a fundamental measure that can be used to judge the general mixing effectiveness of a given PWI. The methods employed in this study to obtain this result naturally motivate the question of whether Φ_∞ can be predicted purely from protocol values. While the majority of the calculated values of the exterior dimension d_{ext} are not equal to 1 or 2, confirming that E on the HS is usually fractal, d_{ext} does not appear to be immediately related to mixing in any practical sense, though this requires further study.

Moving forward, it is important to note that selecting protocols with small nonmixing regions based on Φ_∞ is necessary but not sufficient for efficient mixing with PWIs. This is the case because E is a static feature of PWIs and only represents the possible degree of mixing as $m \to \infty$. It cannot account for all initial conditions, and it does not yield information about the rate of mixing or the rate at which the structure of the dynamics is achieved [52]. Thus, further work is necessary to determine how initial conditions impact mixing and how characteristics of PWIs are related to the rate of mixing, which may require the development of different methods of analysis.

ACKNOWLEDGMENTS

We gratefully acknowledge Jack E. Tumblin and Lachlan D. Smith for insightful discussions. This work was supported by National Science Foundation Grant No. CMMI-1435065.

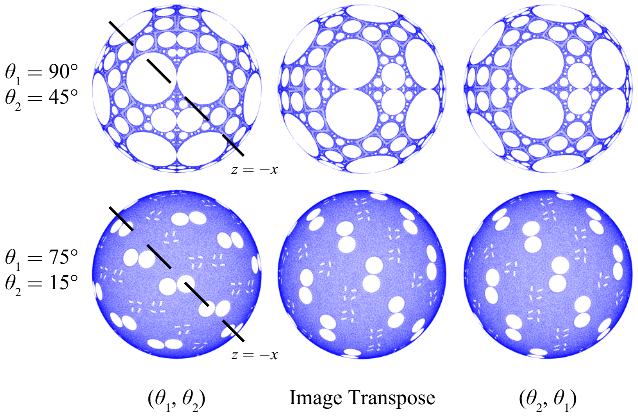

FIG. 14. Comparing E for (θ_1,θ_2) and (θ_2,θ_1) for two different pairs of θ_1 and θ_2 (bottom view). Middle column shows the image transpose of E for (θ_1,θ_2), which is a reflection across $z = -x$ in the coordinate space. The image transpose of E for (θ_1,θ_2) appears identical to E for (θ_2,θ_1).

APPENDIX A: REVERSING SYMMETRY OF E FOR (θ_1,θ_2) AND (θ_2,θ_1)

In Sec. I we noted that there is a symmetry between the structures of E for protocols (θ_1,θ_2) and (θ_2,θ_1). Here we show why this is the case. Consider rotation angles of $\theta_1 = 90^\circ, \theta_2 = 45^\circ$, and $\theta_1 = 75^\circ, \theta_2 = 15^\circ$ shown in Fig. 14. The exceptional set is approximated for protocols (θ_1,θ_2) and (θ_2,θ_1) for both sets of angles in the left and right columns. An image transpose corresponds to reflecting points across the $z = -x$ diagonal in the coordinate space. By transposing the images of E for the (θ_1,θ_2) protocol on the left, we visually confirm that the transpose is the same as the images of E for the (θ_2,θ_1) protocol.

We now investigate whether the progression towards E is the same for protocols (θ_1,θ_2) and (θ_2,θ_1) once the reflection across $z = -x$ is employed, as shown in Fig. 15 for rotation

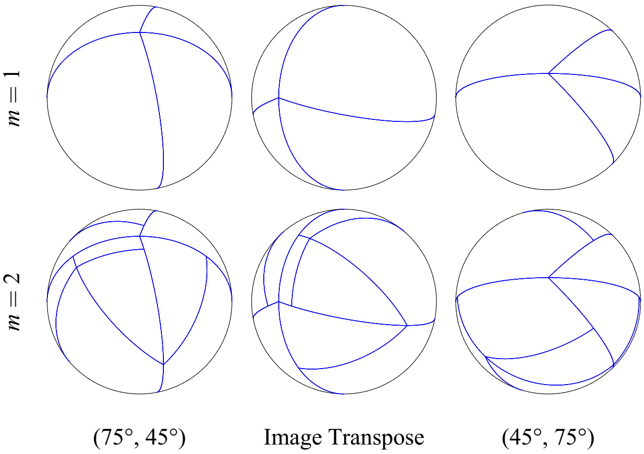

FIG. 15. Comparing the progression towards E for $\theta_1 = 75^\circ$ and $\theta_2 = 45^\circ$ (bottom view). Left column, progression for (θ_1,θ_2); middle column, image transpose of the left column; and right column, progression for (θ_2,θ_1). It is not apparent that the resulting E from both will be the same.

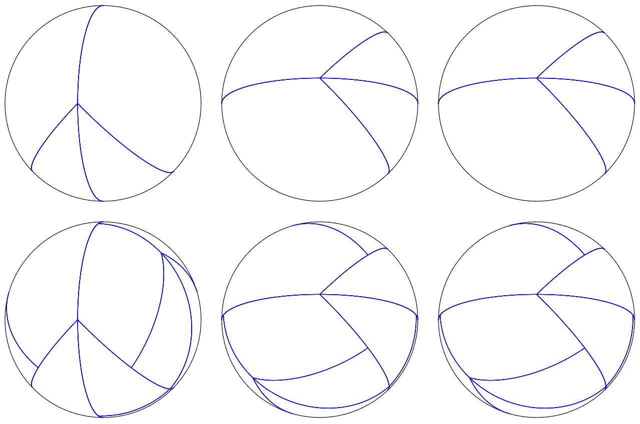

$(75°, 45°)^{-1}$ Image Transpose (45°, 75°)

FIG. 16. Comparing $\mathcal{D}$ (top) and $\mathcal{D} \cup M^{-1}(\mathcal{D})$ (bottom) for the (75°,45°) protocol (left column), their image transpose (middle column), and the progression towards E for the (45°,75°) protocol at $m = 1$ and 2 (bottom view).

angles $\theta_1 = 75°$, $\theta_2 = 45°$. The progressions of (θ_1,θ_2) and (θ_2,θ_1) protocols are not the same in this case, but what is remarkable is that the global features of E for both protocols become the same for large m.

The reason the structures for the (75°,45°) and (45°,75°) protocols are symmetric for large m becomes easier to comprehend if the (θ_1,θ_2) protocol is applied backwards in time, denoted as $(\theta_1,\theta_2)^{-1}$, in which case the rotation by θ_2 comes before the rotation by θ_1, like (θ_2,θ_1), the only difference being that the rotation by θ_2 happens on different axes for the two protocols. We compare $\mathcal{D}$ (top) and $\mathcal{D} \cup M^{-1}(\mathcal{D})$ (bottom) for the (75°,45°) protocol in the left column, its image transpose in the middle column, and the progression for the (45°,75°) protocol in the right column in Fig. 16 and observe that the two structures are the same after one is reflected across $z = -x$. That the set of inverse iterates of $\mathcal{D}$ is also dense in E has been proven for some systems [27–30]. We conjecture that this is also the case here, which is why the structures of E for (θ_1,θ_2) and (θ_2,θ_1) protocols appear symmetric.

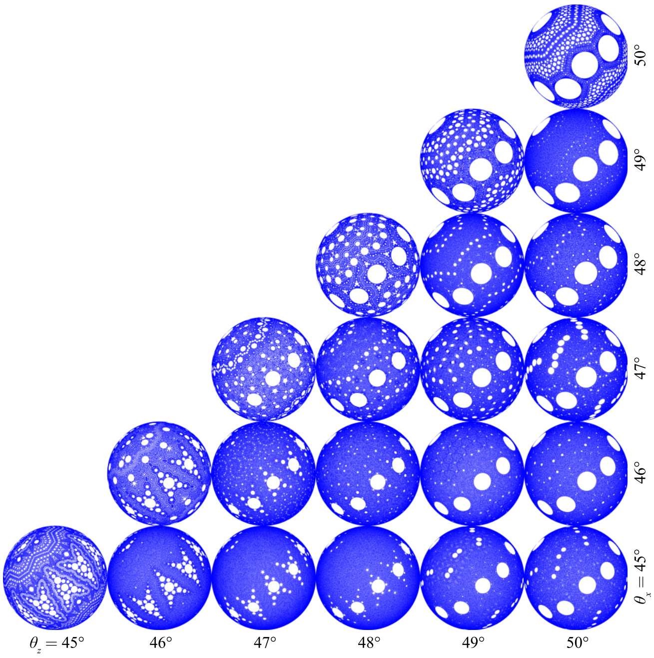

FIG. 18. E for θ_z and $\theta_x \in [45°,50°]$ varying in 1° increments.

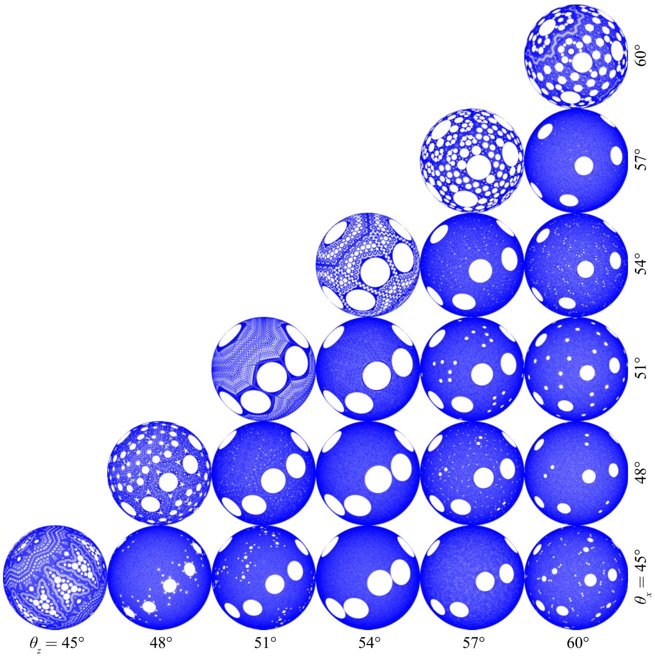

FIG. 17. E for θ_z and $\theta_x \in [45°,60°]$ varying in 3° increments.

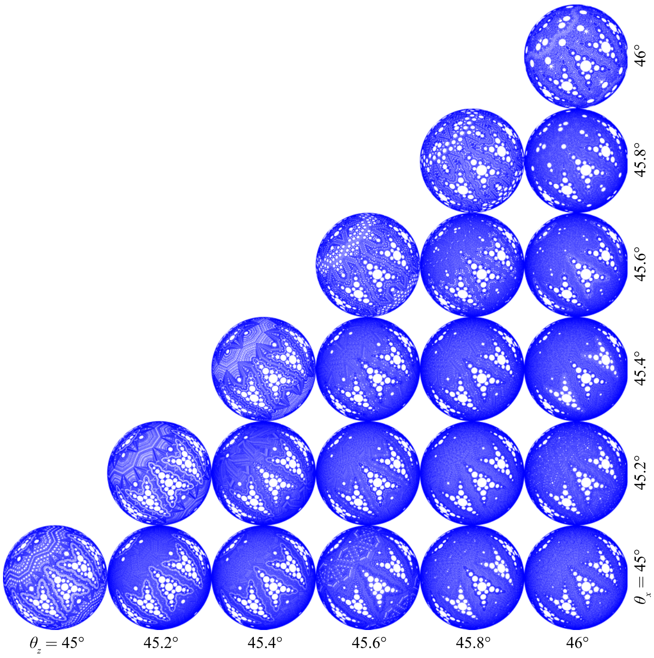

FIG. 19. E for θ_z and $\theta_x \in [45°,46°]$ varying in 0.2° increments.

APPENDIX B: TAXONOMY OF E

As noted in Sec. I, different patterns of E were studied at smaller angular resolutions as shown in Figs. 17–19. While the continuous (θ_z,θ_x) parameter space cannot be fully explored, it is useful to understand the sensitivity of E to the protocol at least in some select areas of the parameter space.

Compared to Fig. 5, Fig. 17 with rotation angles ranging from 45° to 60° in 3° increments shows less variety in patterns, but patterns along the diagonal remain quite distinct from one another. With rotation angles ranging from 45° to 50° in 1° increments (Fig. 18), there appear to be two general features: arrowheads such as those shown for the $(45^\circ,45^\circ)$ protocol, and five large circular cells across the diagonal with an additional large cell in the upper left corner of the HS, as shown for the $(50^\circ,50^\circ)$ protocol. A transition occurs from the arrowhead feature to the five-cell feature in the parameter space between these two protocols as the cell in the center of the arrowhead pattern becomes larger and dwarfs the cells around it, so that the five arrowheads are replaced by five large circular cells.

For rotation angles ranging from 45° to 46°, the arrowhead feature is the most prominent (Fig. 19). Changes in the structure of E are minimal with 0.2° increments in the 45° to 46° range. For protocols on the diagonal, however, their structures of E appear to have finer details (smaller cells) than adjacent protocols.

[1] R. Sturman, Adv. Appl. Mech. **45**, 51 (2012).
[2] G. Juarez, R. M. Lueptow, J. M. Ottino, R. Sturman, and S. Wiggins, Europhys. Lett. **91**, 20003 (2010).
[3] G. Juarez, I. C. Christov, J. M. Ottino, and R. M. Lueptow, Chem. Eng. Sci. **73**, 195 (2012).
[4] S. W. Jones and H. Aref, Phys. Fluids **31**, 469 (1988).
[5] L. D. Smith, M. Rudman, D. R. Lester, and G. Metcalfe, Chaos **26**, 023113 (2016).
[6] S. E. Boyer and D. Elliott, AAPG Bull. **66**, 1196 (1982).
[7] S. W. Golomb, SIAM Rev. **3**, 293 (1961).
[8] M. Keane, Math. Z. **141**, 25 (1975).
[9] M. Keane, Isr. J. Math. **26**, 188 (1977).
[10] W. A. Veech, J. Anal. Math. **33**, 222 (1978).
[11] A. Katok, Isr. J. Math. **35**, 301 (1980).
[12] H. Masur, Ann. Math. **115**, 169 (1982).
[13] D. Aldous and P. Diaconis, Am. Math. Mon. **93**, 333 (1986).
[14] L. N. Trefethen and L. M. Trefethen, Proc. R. Soc. London Ser. A **456**, 2561 (2000).
[15] M. Viana, Rev. Mat. Complut. **19**, 7 (2006).
[16] A. Avila and G. Forni, Ann. Math. **165**, 637 (2007).
[17] R. Sturman, S. W. Meier, J. M. Ottino, and S. Wiggins, J. Fluid Mech. **602**, 129 (2008).
[18] C. F. Novak, J. Mod. Dyn. **3**, 379 (2009).
[19] H. Hmili, Discrete Contin. Dyn. Syst. **27**, 1079 (2010).
[20] M. K. Krotter, I. C. Christov, J. M. Ottino, and R. M. Lueptow, Int. J. Bifurcat. Chaos **22**, 1230041 (2012).
[21] A. Goetz, *Trends in Mathematics: Fractals in Graz 2001* (Birkhaüser Verlag, Basel, 2003), p. 135.
[22] A. Goetz and G. Poggiaspalla, Nonlinearity **17**, 1787 (2004).
[23] X.-C. Fu and J. Duan, Phys. D (Amsterdam, Neth.) **237**, 3369 (2008).
[24] B. Kahng, Chaos **19**, 023115 (2009).
[25] P. P. Park, P. B. Umbanhowar, J. M. Ottino, and R. M. Lueptow, Chaos **26**, 073115 (2016).
[26] I. C. Christov, J. M. Ottino, and R. M. Lueptow, Chaos **20**, 023102 (2010).
[27] J. H. Lowenstein and F. Vivaldi, Nonlinearity **11**, 1321 (1998).
[28] J. H. Lowenstein and F. Vivaldi, Chaos **10**, 747 (2000).
[29] B. Kahng, Ergod. Theor. Dyn. Syst. **22**, 483 (2002).
[30] B. Kahng, Dyn. Syst. **19**, 245 (2004).
[31] A. Goetz, Illinois J. Math. **44**, 465 (2000).
[32] A. Goetz, Nonlinearity **14**, 205 (2001).
[33] D. K. Umberger and J. D. Farmer, Phys. Rev. Lett. **55**, 661 (1985).
[34] J. D. Farmer, E. Ott, and J. A. Yorke, Phys. D (Amsterdam, Neth.) **7**, 153 (1983).
[35] C. Grebogi, S. W. McDonald, E. Ott, and J. A. Yorke, Phys. Lett. A **110**, 1 (1985).
[36] P. Ashwin, Phys. Lett. A **232**, 409 (1997).
[37] K. R. Sreenivasan and C. Meneveau, J. Fluid Mech. **173**, 357 (1986).
[38] J. M. Ottino, C. W. Leong, H. Rising, and P. D. Swanson, Nature (London) **333**, 419 (1988).
[39] E. Ott and T. M. Antonsen, Jr., Phys. Rev. Lett. **61**, 2839 (1988).
[40] K. R. Sreenivasan, R. R. Prasad, C. Mendeveau, and R. Ramshankar, *Fractals in Geophysics* (Birkhaüser Verlag, Basel, 1989), p. 43.
[41] J. M. Ottino, F. J. Muzzio, M. Tjahjadi, J. G. Franjione, S. C. Jana, and H. A. Kusch, Science **257**, 754 (1992).
[42] J. Baldyga and J. R. Bourne, Chem. Eng. Sci. **50**, 381 (1995).
[43] P. E. Dimotakis and H. J. Catrakis, GALCIT Report No. FM97-1, 1997 (unpublished).
[44] G. O. Fountain, D. V. Khakhar, and J. M. Ottino, Science **281**, 683 (1998).
[45] D. Perugini and G. Poli, Earth Planet. Sci. Lett. **175**, 93 (2000).
[46] D. Perugini, G. Poli, and R. Mazzuoli, J. Volcanol. Geotherm. Res. **124**, 255 (2003).
[47] P. V. Danckwerts, Appl. Sci. Res. **3**, 279 (1952).
[48] P. Ashwin, W. Chambers, and G. Petkov, Int. J. Bifurcat. Chaos **7**, 2603 (1997).
[49] L. Wan, T. Wong, and C. Leung, IEEE Trans. Visualization Comput. Graphics **13**, 720 (2007).
[50] T. Coleman and Y. Li, Math. Program. **67**, 189 (1994).
[51] T. Coleman and Y. Li, SIAM J. Optim. **6**, 418 (1996).
[52] S. C. Jana, G. Metcalfe, and J. M. Ottino, J. Fluid Mech. **269**, 199 (1994).